Vector Modulator for W-Band Software Radar Techniques

Douglas S. McPherson, *Member, IEEE,* and Stepan Lucyszyn, *Member, IEEE*

***Abstract*—Direct-carrier modulation is an attractive technique for low-cost high-performance radar transceivers. In this paper, it is shown that, when the technique is applied to a generic homodyne radar architecture, the signaling waveform can be software adapted without requiring any hardware modifications. The key circuit in this novel software radar is a W-band monolithic I–Q vector modulator employing two push–pull (bi-phase) amplitude modulators. To fully exploit this circuit's capacity to generate accurate constellations at millimeter-wave frequencies, a generalized theoretical analysis of the I–Q (push–pull) vector modulator is presented. This is a comprehensive analysis of the topology and does not assume ideal components. As a demonstration of the vector modulator's flexibility, a 76.5-GHz MMIC version has been fabricated and characterized by means of static S-parameter measurements and by several modulation spectra. Based on the theoretical model and the measured results, the I–Q (push–pull) vector modulator promises to be a vital component for the realization of future software radar.**

***Index Terms*—Millimeter-wave integrated circuits, millimeter-wave radar, MMICs, vector modulator, W-band.**

I. Introduction

THE use of direct carrier modulation at millimeter-wave frequencies has recently attracted considerable interest [1]–[5]. Its principal benefits are greatly reduced front-end hardware complexity, lower cost, and increased modulation flexibility. The use of a modulator operating directly at the carrier frequency avoids the need for complex IF mixer, filter, and amplifier chains. Moreover, if a medium power transmitting device (such as a Gunn) is used for the signal source, there may also be no need for expensive RF power amplifiers (PAs) or filters.

In this paper, a robust monolithic-microwave integrated-circuit (MMIC) I–Q vector modulator is presented. The design is based on two independently biased push–pull (bi-phase) amplitude modulators connected in phase quadrature. These, in turn, are each comprised of two basic reflection-type modulators that employ cold FETs as variable resistance terminations. This design has proven very successful up to frequencies as high as 60 GHz and has been demonstrated as a 256-quadrature-amplitutde-modulator (QAM) modulator and small-shift frequency translator [2]–[5]. In all instances, it was found that near-perfect constellations could be generated, provided that the circuit was suitably characterized.

To date, the I–Q (push–pull) vector modulator has only been subjected to a cursory analysis assuming ideal passive components [4]. Although this is sufficient to explain how it operates, it is not very representative of the circuit's actual behavior. In this paper, a rigorous theoretical investigation of the vector modulator is presented. The analysis makes no assumptions with regards to the performance of the circuit's constituent components.

One application for which software radar techniques could prove useful is in the area of automotive collision avoidance. At present, most of the reported MMIC radars employ frequency-modulated carrier wave (FMCW) or frequency-shift keying (FSK) [6]–[9], principally due to their low RF complexity. With the addition of two identical 76.5-GHz vector modulators to the basic FMCW RF chipset, current MMIC designs could generate and detect arbitrary phase/amplitude-modulated waveforms. Using fast baseband waveform generators and flexible digital signal processing (DSP)-based receivers, the signaling format could be adapted without requiring any hardware reconfiguration. This offers considerable advantages as automotive radar conditions can change dramatically with variations in traffic volume, weather, and roadside clutter. By adapting the signaling waveform to suit the operational environment, the radar's performance could be significantly improved.

This software radar concept calls for one vector modulator to be inserted in the transmit channel and another to be inserted in the receive channel. Essentially, the first modulates a fixed frequency oscillator and the second remodulates the signal reflected by the target. If the remodulated signal is then integrated and threshold detected, the result is a cross-correlation receiver. Alternatively, by applying a linear-FM chirp-up modulation to the transmitter and chirp-down to the receiver, the range and velocity will appear as a frequency shift at the output of the second vector modulator. This FMCW mode is highly advantageous because it does not require a linearized voltage-controlled oscillator (VCO). The dual-vector modulator architecture presented here is an entirely new approach for automotive collision avoidance radar.

II. Modeling I–Q (Push–Pull) Vector Modulators

The I–Q (push–pull) vector modulator, shown in Fig. 1, is a passive circuit comprised of three basic circuit elements; namely nine Lange couplers, one in-phase power combiner, and eight cold-FET terminations. Any signal entering the input port

Manuscript received August 8, 2000. This work was supported by the U.K. Engineering and Physical Sciences Research Council under Grant GR/L37595.

D. S. McPherson was with the Microwave and Systems Research Group, Department of Electronic Engineering, University of Surrey, Surrey GU2 7XH, U.K. He is now with Quake Technologies Inc., Ottawa, ON, Canada K2K 2TB.

S. Lucyszyn is with the Microwave and Systems Research Group, Department of Electronic Engineering, University of Surrey, Surrey GU2 7XH, U.K.

Publisher Item Identifier S 0018-9480(01)05061-X.

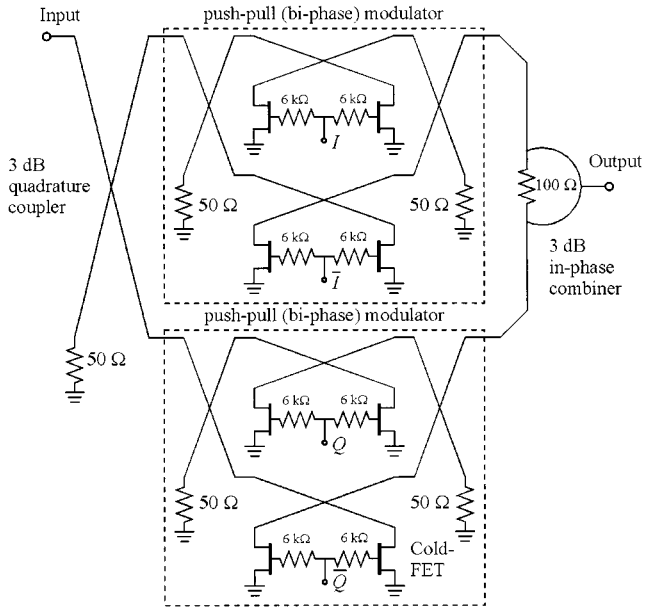

Fig. 1. Schematic of the I–Q (push–pull) vector modulator.

is split into two orthogonal (i.e., I and Q) channels and modulated independently by two push–pull (bi-phase) amplitude modulators [4], [5]. The resulting signals are then recombined in-phase at the output. Although the I–Q (push–pull) vector modulator may appear to be a standard four-channel topology, it is actually a passive two-channel design. As such, its transfer function can assume any arbitrary complex value subject only to a minimum theoretical insertion loss of 6 dB. Due to losses and imperfections in the components, the minimum insertion loss can be much higher. In order to fully explain the deviation from ideality, it is necessary to investigate the circuit in greater detail.

A. Cold Pseudomorphic High-Electron-Mobility Transistor Characterization

A variable resistance element that is readily available in millimeter-wave MMIC technology is the cold pseudomorphic high electron-mobility transistor (pHEMT). This is simply a standard common-source pHEMT device with zero dc bias applied to the drain. By applying a variable voltage to the gate terminal, the extent of the depletion region within the channel can be varied, giving rise to high and low drain–source resistance. For a GaAs depletion mode device, the highest resistance will occur when the channel is pinched off under a strong reverse bias and the lowest resistance will occur when the gate is forward biased. The principle advantages of using this device as a variable resistance are that it requires no dc control current, can be switched very quickly, and requires no special fabrication techniques over and above those that are required for a standard pHEMT process.

Ideally, the cold pHEMT should behave as a pure voltage-controlled resistance, with a range between zero and infinity. In practice, and especially at W-band, the device is observed

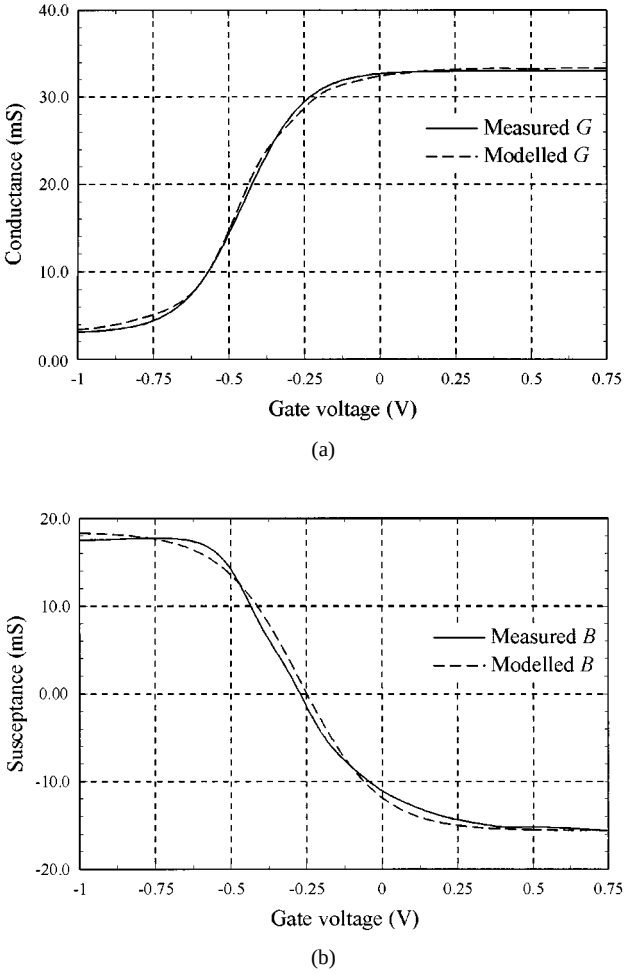

Fig. 2. Measured and modeled cold pHEMT admittance parameters as a function of gate bias: (a) conductance and (b) susceptance.

to have a significant "ON"-state resistance and "OFF"-state capacitive reactance. These effects are readily explained by skin-effect losses in the contacts and channel and charge separation between the drain and source terminals at pinchoff. Both impact heavily on the vector modulator's minimum insertion loss.

The devices used for this study were fabricated by Marconi Caswell Limited, Caswell, U.K., using their 0.25-μm gate-length H40 AlGaAs/InGaAs pHEMT foundry process. The gates of the cold pHEMTs consist of two fingers, each of which is 60-μm wide. This gate geometry was chosen because it offers the best compromise between low OFF-state capacitive reactance and low ON-state resistance. Fig. 2 shows the variation in drain–source admittance with gate bias for the device at 76.5 GHz, as derived from one-port S-parameter measurements. By expressing the S-parameters in terms of admittance, it is relatively simple to fit empirical curves to the real and imaginary components

$$G(V) = 0.015 \tanh\left[5(V + 0.45)\right] + 0.018 \quad (1)$$

$$B(V) = -0.017 \tanh\left[3.9(V + 0.27)\right] + 0.0014. \quad (2)$$

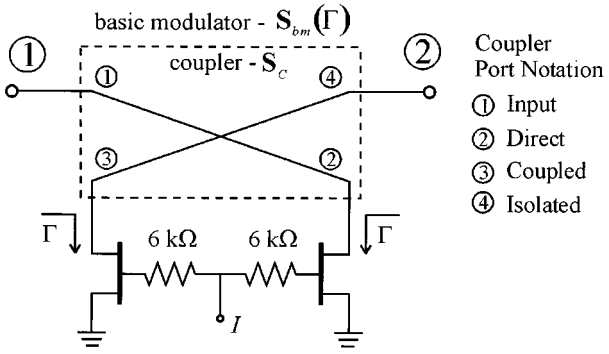

Fig. 3. Schematic of the basic bi-phase reflection-type modulator.

Hence, the termination's bias-dependent reflection coefficient becomes

$$\Gamma(V) = \frac{Y_0 - G(V) - jB(V)}{Y_0 + G(V) + jB(V)}. \tag{3}$$

B. Basic Reflection-Type Modulator

A basic bi-phase reflection-type amplitude modulator is shown in Fig. 3. It consists of two cold pHEMTs connected to the coupled and direct ports of a 50 -Ω directional coupler. When a signal enters the input port of the coupler, it is divided into two equiamplitude, but orthogonal components. A portion of these components is then reflected back into the coupler by the drain–source terminals of the cold pHEMTs. If the gate–source bias of both devices is varied identically, a low drain–source resistance will result in a strong reflection with a 180° phase shift. As the resistance is raised, the magnitude of the reflected component will drop to zero when it reaches 50 Ω. As the resistance is further increased, the reflected component will increase again, but this time without any phase inversion. Assuming ideal couplers, the reflected components will sum at the coupler's isolated port and cancel perfectly at the input port.

Previous analysis of the basic reflection-type modulator and, indeed, the entire vector modulator, has assumed that quadrature couplers are ideal [4], [10]. From measurements of W-band Lange couplers made at the University of Surrey, Surrey, U.K., this assumption has proved invalid. Such couplers have been observed to exhibit isolation as low as 11 dB and can be undercoupled by as much as 1 dB. This occurs because, as the operating frequency increases, the length of the couplers decreases unacceptably with respect to the width and spacing of the interdigitated fingers. Furthermore, underpasses or air bridges become proportionally larger, and have a more pronounced effect on the coupler's overall performance.

A useful model for the Lange couplers can be derived from elementary coupled-line theory. Although it may not be an entirely accurate representation at W-band, it can still yield some insight into how the parameters of the coupled lines affect the vector modulator's performance. Alternatively, if accurate multiport measurement techniques are employed (see, e.g., [11]), the actual S-parameters of the directional couplers can be used instead of the model. From coupled-line theory [12], the even- and odd-mode responses of a completely symmetrical coupler are given by

$$S_{e11}(=S_{e22}) = \frac{j\left(\frac{Z_{0e}}{Z_{0c}} - \frac{Z_{0c}}{Z_{0e}}\right)\sin(\beta l)}{2\cos(\beta l) + j\left(\frac{Z_{0e}}{Z_{0c}} + \frac{Z_{0c}}{Z_{0e}}\right)\sin(\beta l)} \tag{4}$$

$$S_{e21}(=S_{e12}) = \frac{2}{2\cos(\beta l) + j\left(\frac{Z_{0e}}{Z_{0c}} + \frac{Z_{0c}}{Z_{0e}}\right)\sin(\beta l)} \tag{5}$$

$$S_{o11}(=S_{o22}) = \frac{j\left(\frac{Z_{0o}}{Z_{0c}} - \frac{Z_{0c}}{Z_{0o}}\right)\sin(\beta l)}{2\cos(\beta l) + j\left(\frac{Z_{0o}}{Z_{0c}} + \frac{Z_{0c}}{Z_{0o}}\right)\sin(\beta l)} \tag{6}$$

$$S_{o21}(=S_{o12}) = \frac{2}{2\cos(\beta l) + j\left(\frac{Z_{0o}}{Z_{0c}} + \frac{Z_{0c}}{Z_{0o}}\right)\sin(\beta l)} \tag{7}$$

where Z_{0e}, Z_{0o}, and Z_{0c} are the even mode, odd mode, and characteristic impedances of the coupler, and βl is the electrical length of the coupled section. The even- and odd-mode responses are combined to give two partial matrices

$$\mathbf{S}_a = \begin{bmatrix} \frac{S_{e11} + S_{o11}}{2} & \frac{S_{e21} + S_{o21}}{2} \\ \frac{S_{e21} + S_{o21}}{2} & \frac{S_{e11} + S_{o11}}{2} \end{bmatrix} \tag{8}$$

$$\mathbf{S}_b = \begin{bmatrix} \frac{S_{e11} - S_{o11}}{2} & \frac{S_{e21} - S_{o21}}{2} \\ \frac{S_{e21} - S_{o21}}{2} & \frac{S_{e11} - S_{o11}}{2} \end{bmatrix} \tag{9}$$

which, in turn, are assembled into the complete S-parameter matrix

$$\mathbf{S}_c = \begin{bmatrix} [\mathbf{S}_a] & [\mathbf{S}_b] \\ [\mathbf{S}_b] & [\mathbf{S}_a] \end{bmatrix} = \begin{bmatrix} S_{c11} & S_{c21} & S_{c31} & S_{c41} \\ S_{c21} & S_{c11} & S_{c41} & S_{c31} \\ S_{c31} & S_{c41} & S_{c11} & S_{c21} \\ S_{c41} & S_{c31} & S_{c21} & S_{c11} \end{bmatrix}. \tag{10}$$

Referring to Fig. 3, the response of the basic reflection-type modulator is derived by terminating ports 2 and 3 of the coupler with identical terminations. The reflection coefficient of the terminations is given by Γ. Having done this, the four-port can then be reduced to an equivalent two-port using the well-known port-reduction technique of [12]. This yields the S-parameters of the basic modulator scattering matrix, $\mathbf{S}_{bm}(\Gamma)$, shown in (11) and (12) at the bottom of the following page. For an ideal coupler, it can be readily shown that (11) reduces to zero and (12) reduces to $-j\Gamma$. This latter result clearly indicates that the impedance variation of the cold pHEMTs plays an important role in establishing the minimum insertion loss of the modulator. Equally significant is the effect of having nonzero coupler isolation (i.e., $S_{c41} \neq 0$). As will be seen in Section V, insufficient isolation presents a clear leakage path that will degrade the vector modulator's ability to suppress the carrier. Equations (11) and (12) also express the effects of amplitude and phase imbalances and imperfect coupler matching on the basic modulator performance.

C. Push–Pull (Bi-Phase) Modulator

Ideally, for pHEMT devices with a large resistance variation and a small capacitance variation, the basic reflection-type modulator is capable of full bi-phase operation with negligible insertion phase variation. However, when the OFF-state capacitance and the minimum ON-state resistance are significant, the insertion phase will be nonzero and the minimum insertion loss will be poor. If two basic reflection-type modulators are arranged in a push–pull configuration, between two quadrature couplers, the insertion phase variation can be minimized, the minimum insertion loss improved, and bi-phase operation largely restored [4], [5]. From the dashed boxes of Fig. 1, this configuration appears similar to the arrangement used for a balanced amplifier. For the push–pull mode, however, the output is taken from the isolation port and the two basic modulators are supplied with complementary control signals. The summation of the two complementary responses yields a much larger ON–OFF impedance variation. Previous analysis, that has assumed ideal couplers, indicates that the overall push–pull transmission response is half of the difference between the transmission responses of the two basic modulators, when they are supplied with complementary control signals. In practice, the finite isolation and impedance mismatch of the couplers complicates this arrangement, by allowing reflected signals from each of the two basic modulators to pass into one another. Calculating the S-parameters of the push–pull (bi-phase) modulator involves cascading three four-port networks. In the first instance, the input coupler must be cascaded with the basic modulator pair. The corresponding 4×4 matrices, shown in Fig. 4(a), are $\mathbf{S}'_c$ for the input coupler and $\mathbf{S}_{bp}(\Gamma)$ for the basic modulator pair

$$\mathbf{S}'_c = \begin{bmatrix} S_{c11} & S_{c41} & S_{c31} & S_{c21} \\ S_{c41} & S_{c11} & S_{c21} & S_{c31} \\ S_{c31} & S_{c21} & S_{c11} & S_{c41} \\ S_{c21} & S_{c31} & S_{c41} & S_{c11} \end{bmatrix} \tag{13}$$

$$\mathbf{S}_{bp}(\Gamma) = \begin{bmatrix} S_{bm}(\Gamma)_{11} & 0 & S_{bm}(\Gamma)_{21} & 0 \\ 0 & S_{bm}(\overline{\Gamma})_{11} & 0 & S_{bm}(\overline{\Gamma})_{21} \\ S_{bm}(\Gamma)_{21} & 0 & S_{bm}(\Gamma)_{11} & 0 \\ 0 & S_{bm}(\overline{\Gamma})_{21} & 0 & S_{bm}(\overline{\Gamma})_{11} \end{bmatrix}. \tag{14}$$

The prime notation added to $\mathbf{S}_c$ in (13) signifies that ports 2 and 4 of the quadrature coupler have been interchanged. This change is necessitated by the notation requirements for cascading n-port networks. In (14), $\overline{\Gamma}$ is the complementary reflection coefficient of Γ. A pair of reflection coefficients (and their required bias levels, V and $\overline{V}$) are said to be complementary when they give $\Gamma(V) = -\overline{\Gamma}(\overline{V})$.

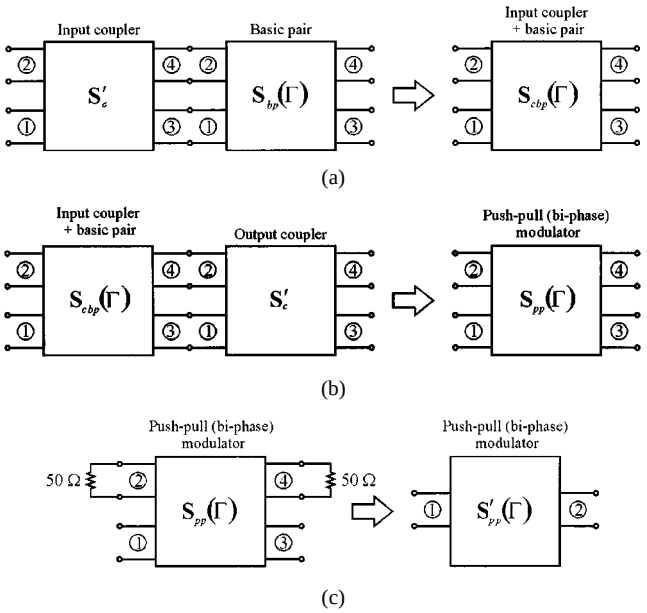

Fig. 4. Networks used to calculate the response of the push–pull (bi-phase) modulator: (a) input coupler cascaded with basic modulator pair, (b) input coupler and basic modulator pair cascaded with output coupler, and (c) final push–pull (bi-phase) modulator.

The matrices in (13) and (14) must now be partitioned into four two-port networks. Since there are only two distinct partitioned pairs for each matrix, the duplicates are omitted and the resultants identified by their four-port name. Indexes of 11 and 12 are used to indicate where the partitions were in their original 4×4 matrix

$$\mathbf{S}'_{c11} = \begin{bmatrix} S_{c11} & S_{c41} \\ S_{c41} & S_{c11} \end{bmatrix}$$
$$\mathbf{S}'_{c12} = \begin{bmatrix} S_{c31} & S_{c21} \\ S_{c21} & S_{c31} \end{bmatrix} \tag{15}$$

$$\mathbf{S}_{bp11}(\Gamma) = \begin{bmatrix} S_{bm}(\Gamma)_{11} & 0 \\ 0 & S_{bm}(\overline{\Gamma})_{11} \end{bmatrix}$$
$$\mathbf{S}_{bp12}(\Gamma) = \begin{bmatrix} S_{bm}(\Gamma)_{21} & 0 \\ 0 & S_{bm}(\overline{\Gamma})_{21} \end{bmatrix}. \tag{16}$$

$$S_{bm}(\Gamma)_{11} = S_{bm}(\Gamma)_{22} = S_{c11} + \frac{2S_{c21}S_{c31}S_{c41}\left(\frac{\Gamma}{1-S_{c11}\Gamma}\right)^2 + \left(S_{c21}^2 + S_{c31}^2\right)\left(\frac{\Gamma}{1-S_{c11}\Gamma}\right)}{1-\left(\frac{S_{c41}\Gamma}{1-S_{c11}\Gamma}\right)^2} \tag{11}$$

$$S_{bm}(\Gamma)_{21} = S_{bm}(\Gamma)_{12} = S_{c41} + \frac{2S_{c21}S_{c31}\left(\frac{\Gamma}{1-S_{c11}\Gamma}\right) + \left(S_{c21}^2 + S_{c31}^2\right)S_{c41}\left(\frac{\Gamma}{1-S_{c11}\Gamma}\right)^2}{1-\left(\frac{S_{c41}\Gamma}{1-S_{c11}\Gamma}\right)^2} \tag{12}$$

Using the expressions for cascading n-port networks [12], a new set of partitioned scattering matrices is obtained. These are part of $\mathbf{S}_{cbp}(\Gamma)$, a four-port consisting of the input coupler and the basic modulator pair

$$\mathbf{S}_{cbp11}(\Gamma) = \mathbf{S}'_{c11} + \mathbf{S}'_{c12}\Big[\mathbf{I} - \mathbf{S}_{bp11}(\Gamma)\mathbf{S}'_{c11}\Big]^{-1}\mathbf{S}_{bp11}(\Gamma)\mathbf{S}'_{c12} \tag{17}$$

$$\begin{aligned}\mathbf{S}_{cbp12}(\Gamma) &= \Big[\mathbf{S}_{cbp21}(\Gamma)\Big]^T \\ &= \mathbf{S}'_{c12}\Big[\mathbf{I} - \mathbf{S}_{bp11}(\Gamma)\mathbf{S}'_{c11}\Big]^{-1}\mathbf{S}_{bp12}(\Gamma)\end{aligned} \tag{18}$$

$$\begin{aligned}\mathbf{S}_{cbp22}(\Gamma) &= \mathbf{S}_{bp11}(\Gamma) + \mathbf{S}_{bp12}(\Gamma)\Big[\mathbf{I} - \mathbf{S}'_{c11}\mathbf{S}_{bp11}(\Gamma)\Big]^{-1} \\ &\quad \cdot \mathbf{S}'_{c11}\mathbf{S}_{bp12}(\Gamma).\end{aligned} \tag{19}$$

In the above expressions, $\mathbf{I}$ is the identity matrix, $[\ ]^{-1}$ signifies the matrix inverse, and $[\ ]^T$ signifies the matrix transpose. Having done this, it is now possible to derive the scattering matrix for the entire push–pull modulator $\mathbf{S}_{pp}(\Gamma)$ by cascading the new four-port $\mathbf{S}_{cbp}(\Gamma)$ with the output four-port coupler $\mathbf{S}'_c$. This step, which is illustrated in Fig. 4(b), yields a set of equations similar in form to (17)–(19)

$$\begin{aligned}\mathbf{S}_{pp11}(\Gamma) &= \mathbf{S}_{pp22}(\Gamma) \\ &= \mathbf{S}_{cbp11}(\Gamma) + \mathbf{S}_{cbp12}(\Gamma)\Big[\mathbf{I} - \mathbf{S}'_{c11}\mathbf{S}_{cbp22}(\Gamma)\Big]^{-1} \\ &\quad \cdot \mathbf{S}'_{c11}\mathbf{S}_{cbp12}(\Gamma)\end{aligned} \tag{20}$$

$$\begin{aligned}\mathbf{S}_{pp12}(\Gamma) &= \mathbf{S}_{pp21}(\Gamma) \\ &= \mathbf{S}_{cbp12}(\Gamma)\Big[\mathbf{I} - \mathbf{S}'_{c11}\mathbf{S}_{cbp22}(\Gamma)\Big]^{-1}\mathbf{S}'_{c12}.\end{aligned} \tag{21}$$

Since ports 2 and 4 of the push–pull modulator are terminated in 50 -Ω loads, $\mathbf{S}_{pp}(\Gamma)$ can be reduced to an equivalent two-port network by extracting the upper leftmost S-parameters of the four partitions given in (20) and (21). Referring to Fig. 4(c), the reduced scattering matrix for the push–pull modulator is

$$\mathbf{S}'_{pp}(\Gamma) = \begin{bmatrix} S_{pp11}(\Gamma)_{11} & S_{pp12}(\Gamma)_{11} \\ S_{pp12}(\Gamma)_{11} & S_{pp11}(\Gamma)_{11} \end{bmatrix}. \tag{22}$$

D. Complete Vector Modulator

The complete I–Q vector modulator is realized by splitting the input signal into orthogonal channels, modulating each one independently, and summing the resultant. Since both independent push–pull modulators are bi-phase, they can be used to form the axes of a two-dimensional space that spans all four transmission vector quadrants. Summing is achieved using an in-phase power combiner. Mathematically, the procedure for determining the overall vector modulator response is very similar to that used for the push–pull modulator. Referring to (14), the entries for the two basic modulators are now replaced by the S-parameters for two push–pull modulators with terminations

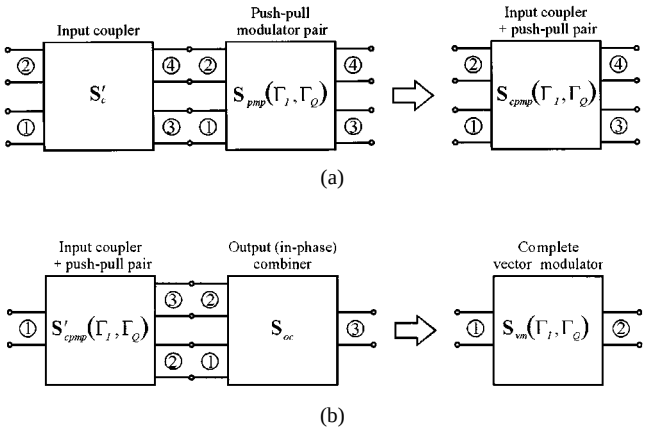

Fig. 5. Networks used to calculate the response of the complete vector modulator: (a) input coupler cascaded with push–pull (bi-phase) modulator pair and (b) input coupler and push–pull pair cascaded with output (in-phase) combiner.

adjusted to Γ_I and Γ_Q, respectively. If this matrix is partitioned as in (16), the resulting submatrices of the push–pull modulator pair (*pmp*) become

$$\begin{aligned}\mathbf{S}_{pmp11}(\Gamma_I, \Gamma_Q) &= \begin{bmatrix} S_{pp11}(\Gamma_I)_{11} & 0 \\ 0 & S_{pp11}(\Gamma_Q)_{11} \end{bmatrix} \\ \mathbf{S}_{pmp12}(\Gamma_I, \Gamma_Q) &= \begin{bmatrix} S_{pp12}(\Gamma_I)_{11} & 0 \\ 0 & S_{pp12}(\Gamma_Q)_{11} \end{bmatrix}.\end{aligned} \tag{23}$$

To determine the scattering matrix of the combined input coupler and *pmp*, the four-port cascade technique must be applied once again. As shown in Fig. 5(a), the first matrix is given by $\mathbf{S}'_c$ and the second is represented by its partitions in (23). The complete four-port S-parameter description of the cascaded network $\mathbf{S}_{cpmp}(\Gamma_I, \Gamma_Q)$ is given by a new set of partitions

$$\begin{aligned}&\mathbf{S}_{cpmp11}(\Gamma_I, \Gamma_Q) \\ &\quad = \mathbf{S}'_{c11} + \mathbf{S}'_{c12}\Big[\mathbf{I} - \mathbf{S}_{pmp11}(\Gamma_I, \Gamma_Q)\mathbf{S}'_{c11}\Big]^{-1} \\ &\qquad \cdot \mathbf{S}_{pmp11}(\Gamma_I, \Gamma_Q)\mathbf{S}'_{c12}\end{aligned} \tag{24}$$

$$\begin{aligned}&\mathbf{S}_{cpmp12}(\Gamma_I, \Gamma_Q) \\ &\quad = \Big[\mathbf{S}_{cpmp21}(\Gamma_I, \Gamma_Q)\Big]^T \\ &\quad = \mathbf{S}'_{c12}\Big[\mathbf{I} - \mathbf{S}_{pmp11}(\Gamma_I, \Gamma_Q)\mathbf{S}'_{c11}\Big]^{-1}\mathbf{S}_{pmp12}(\Gamma_I, \Gamma_Q)\end{aligned} \tag{25}$$

$$\begin{aligned}&\mathbf{S}_{cpmp22}(\Gamma_I, \Gamma_Q) \\ &\quad = \mathbf{S}_{pmp11}(\Gamma_I, \Gamma_Q) + \mathbf{S}_{pmp12}(\Gamma_I, \Gamma_Q) \\ &\qquad \cdot \Big[\mathbf{I} - \mathbf{S}'_{c11}\mathbf{S}_{pmp11}(\Gamma_I, \Gamma_Q)\Big]^{-1}\mathbf{S}'_{c11}\mathbf{S}_{pmp12}(\Gamma_I, \Gamma_Q).\end{aligned} \tag{26}$$

Ports 3 and 4 of the combined input coupler and pmp can now be summed using a three-port in-phase combiner. To do so, port 2 must first be terminated by a 50-Ω load and $\mathbf{S}_{cpmp}(\Gamma_I, \Gamma_Q)$

represented as a three-port network. The reduced matrix $\mathbf{S}'_{cpmp}(\Gamma_I, \Gamma_Q)$ is then partitioned as follows:

$$\mathbf{S}'_{cpmp11}(\Gamma_I,\Gamma_Q) = \Big[S_{cpmp11}(\Gamma_I,\Gamma_Q)_{11}\Big]$$
$$\mathbf{S}'_{cpmp12}(\Gamma_I,\Gamma_Q) = \Big[S_{cpmp12}(\Gamma_I,\Gamma_Q)_{11} \quad S_{cpmp12}(\Gamma_I,\Gamma_Q)_{12}\Big]$$
$$\mathbf{S}'_{cpmp21}(\Gamma_I,\Gamma_Q) = \begin{bmatrix} S_{cpmp21}(\Gamma_I,\Gamma_Q)_{11} \\ S_{cpmp21}(\Gamma_I,\Gamma_Q)_{21} \end{bmatrix}$$
$$\mathbf{S}'_{cpmp22}(\Gamma_I,\Gamma_Q) = \Big[S_{cpmp22}(\Gamma_I,\Gamma_Q)_{11}\Big]. \tag{27}$$

For the three-port output (in-phase) combiner, the partitioned submatrices are defined in terms of S-parameters assuming port 3 is the signal combining port

$$\mathbf{S}_{oc11} = \begin{bmatrix} S_{oc22} & S_{oc23} \\ S_{oc32} & S_{oc33} \end{bmatrix}$$
$$\mathbf{S}_{oc12} = \begin{bmatrix} S_{oc21} \\ S_{oc31} \end{bmatrix}$$
$$\mathbf{S}_{oc21} = \Big[S_{oc12} \quad S_{oc13}\Big]$$
$$\mathbf{S}_{oc22} = \Big[S_{oc11}\Big]. \tag{28}$$

The overall I–Q vector modulator response is now determined by cascading the two three-ports of Fig. 5(b) to obtain the final scattering matrix $\mathbf{S}_{vm}(\Gamma_I, \Gamma_Q)$. Its S-parameters are given by

$$S_{vm11}(\Gamma_I, \Gamma_Q) = \mathbf{S}'_{cpmp11}(\Gamma_I, \Gamma_Q) + \mathbf{S}'_{cpmp12}(\Gamma_I, \Gamma_Q) \cdot \Big[\mathbf{I} - \mathbf{S}_{oc11}\mathbf{S}'_{cpmp22}(\Gamma_I, \Gamma_Q)\Big]^{-1} \mathbf{S}_{oc11}\mathbf{S}'_{cpmp21}(\Gamma_I, \Gamma_Q) \tag{29}$$

$$S_{vm12}(\Gamma_I, \Gamma_Q) = \mathbf{S}_{vm21}(\Gamma_I, \Gamma_Q) = \mathbf{S}'_{cpmp12}(\Gamma_I, \Gamma_Q)\Big[\mathbf{I} - \mathbf{S}_{oc11}\mathbf{S}'_{cpmp22}(\Gamma_I, \Gamma_Q)\Big]^{-1}\mathbf{S}_{oc12} \tag{30}$$

$$S_{vm22}(\Gamma_I, \Gamma_Q) = \mathbf{S}_{oc22} + \mathbf{S}_{oc21}\Big[\mathbf{I} - \mathbf{S}'_{cpmp22}(\Gamma_I, \Gamma_Q)\mathbf{S}_{oc11}\Big]^{-1} \cdot \mathbf{S}'_{cpmp22}(\Gamma_I, \Gamma_Q)\mathbf{S}_{oc12}. \tag{31}$$

Equations (29)–(31) give a full description of the vector modulators behavior and account for all of the imperfections present in the quadrature couplers and the output (in-phase) combiner. For ideal components matched to 50 Ω, the expressions can be greatly simplified as follows:

$$S_{vm11}(\Gamma_I, \Gamma_Q) = S_{vm22}(\Gamma_I, \Gamma_Q) = 0 \tag{32}$$

$$S_{vm21}(\Gamma_I, \Gamma_Q) = S_{vm12}(\Gamma_I, \Gamma_Q) = -\frac{1}{4}\Big[\Big(\Gamma_I - \overline{\Gamma}_I\Big) + j\Big(\Gamma_Q - \overline{\Gamma}_Q\Big)\Big]. \tag{33}$$

Equation (33) is an important result because it clearly illustrates how the vector modulator's transmission response is dependent on the range of reflection coefficient values assumed by the terminations. For ideal complementary terminations (i.e., $\Gamma_I = -\overline{\Gamma}_I$ and $\Gamma_Q = -\overline{\Gamma}_Q$), it can be further reduced to

$$S_{vm21}(\Gamma_I, \Gamma_Q) = S_{vm12}(\Gamma_I, \Gamma_Q) = -\frac{1}{2}\Big[\Gamma_I + j\Gamma_Q\Big]. \tag{34}$$

Thus, assuming perfect components (including $|\Gamma_{I,Q}| \leq 1$), the minimum inherent insertion loss for the I–Q (push–pull) vector modulator is 6 dB. This is consistent with the expected behavior of a two-channel passive vector modulator.

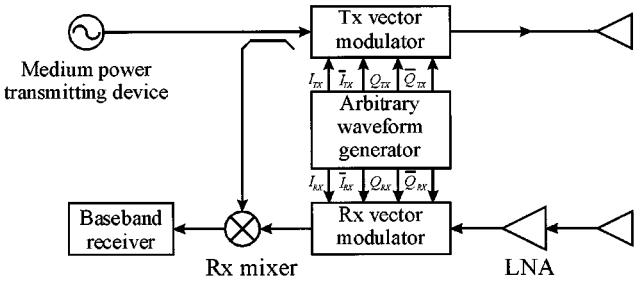

Fig. 6. Proposed software radar including transmitter and receiver vector modulators.

III. Application to 76.5-GHz Radar Systems

At present, the majority of reported 76.5-GHz radar chipsets [6]–[9] consist of several fundamental building blocks, namely: 1) a stabilized signal source; 2) a directional coupler; 3) a PA; 4) a low-noise amplifier (LNA); and 5) a mixer. If two vector modulators are added to this basic chipset, the radar can be software adapted, using an arbitrary baseband waveform generator and DSP-based receiver, to employ any number of modulation formats including FMCW, FSK, pulsed FM, pulsed AM, and/or polyphase code. Given that a medium power transmitting device (such as a Gunn) is used as a fixed-frequency source, it may even be possible to omit using a PA and an output filter. The potential applications of this software transceiver architecture are by no means limited only to automotive radar. Indeed, similar proposals have been made for millimeter-wave software radios [3].

A schematic of the software radar is shown in Fig. 6. Essentially, one vector modulator is used to generate a radar signal and a second is used, in conjunction with a DSP baseband integrator and threshold detector, to form a cross-correlation receiver. To appreciate the architecture, consider an arbitrarily modulated continuous wave (CW) waveform

$$v(t) = A(t)\cos\Big[\omega t + \theta(t)\Big]. \tag{35}$$

Expanding it into I and Q components

$$v(t) = \frac{A(t)}{\sqrt{2}}\cos\Big[\theta(t)\Big]\cos(\omega t) - \frac{A(t)}{\sqrt{2}}\sin\Big[\theta(t)\Big]\sin(\omega t). \tag{36}$$

To apply this modulation to the I–Q (push–pull) vector modulator, the baseband I and Q signals (and their complements) must be predistorted to correct for the nonlinear relationship between the drain–source impedance and applied gate bias of the cold pHEMTs. The resulting waveform is then transmitted and received some time τ later and remodulated by the reference modulator. This is the first requirement for a cross-correla-

tion receiver, whereby the transmitted modulation is effectively being compared to a stored replica. After some manipulation, the input to the receiver mixer is

$$v_{RX}(t) = \frac{A(t)A(t-\tau)}{\sqrt{2}}\cos\Big[\theta(t)\Big]\cos\Big[\omega(t-\tau)+\theta(t-\tau)\Big] - \frac{A(t)A(t-\tau)}{\sqrt{2}}\sin\Big[\theta(t)\Big]\sin\Big[\omega(t-\tau)+\theta(t-\tau)\Big]. \quad (37)$$

Downconverting to baseband gives

$$v_{BB}(t) = \frac{A(t)A(t-\tau)}{2\sqrt{2}}\cos\Big\{\omega\tau - \big[\theta(t)+\theta(t-\tau)\big]\Big\}. \quad (38)$$

To complete the correlation of the transmitted signal with the received signal, the baseband output should now be low-pass filtered or integrated and dumped to a threshold detector. The signal seen by the threshold detector at time T is

$$v_{\rm det}(t) = \frac{1}{2\sqrt{2}}\int_0^T A(t)A(t-\tau) \cdot\cos\Big\{\omega\tau - \big[\theta(t)+\theta(t-\tau)\big]\Big\}dt. \quad (39)$$

The receiver then adjusts the relative delays between the transmitter and receiver modulation patterns to test for the presence of a target. When the output of (39) is maximized, an estimate of range can be extracted. Automatic gain control is provided by scaling the amplitude response of the receiver vector modulator.

Using the same hardware components as shown in Fig. 6, the software radar can be adapted to operate in an FMCW mode. This is achieved by reprogramming the baseband waveform generator to output chirp-up modulation for the transmitter and chirp-down for the receiver. In addition, the integrator and threshold detector are replaced by a fast Fourier transform (FFT) detector. Since both of these baseband functions can be realized using the same DSP, only a software change is required to switch between them. The principle of the FMCW mode is to remodulate the incoming signal with a quadratic phase term that is opposite in sign to that used in the transmitter. This has the effect of removing the chirp modulation. The required modulation terms for this operation are

$$A(t) = A(t-\tau) = 1$$
$$\theta(t) = \frac{-\mu t^2}{2}$$
$$\theta(t-\tau) = \frac{\mu(t-\tau)^2}{2} \quad (40)$$

where "μ" is the frequency ramp rate for linear FM. Substituting these terms into (38), the baseband output becomes

$$v_{BB}(t) = \frac{1}{2\sqrt{2}}\cos\left(\omega\tau + \mu t\tau - \frac{\mu\tau^2}{2}\right) \quad (41)$$

which is the beat signal for two time-shifted linear FM waveforms. The beat frequency $f_{\rm IF} = \mu\tau/2\pi$ is directly related to the range $R = \pi f_{\rm IF}c/\mu$. This FMCW mode is, itself, quite advantageous because it only requires a fixed-frequency oscillator and is capable of generating an exceptionally linear frequency ramp [13].

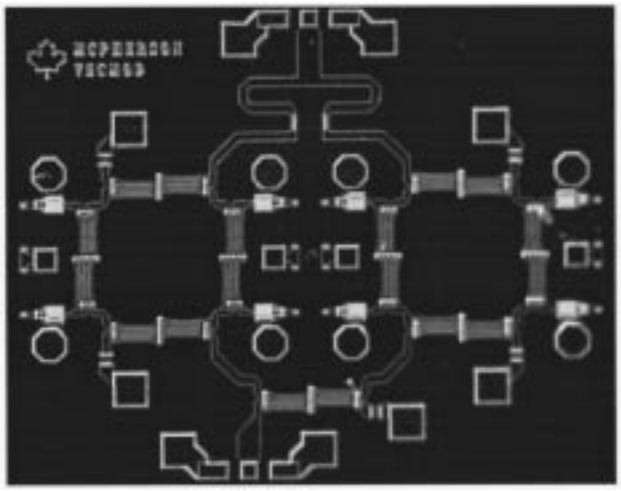

Fig. 7. Microphotograph of the MMIC I–Q (push–pull) vector modulator.

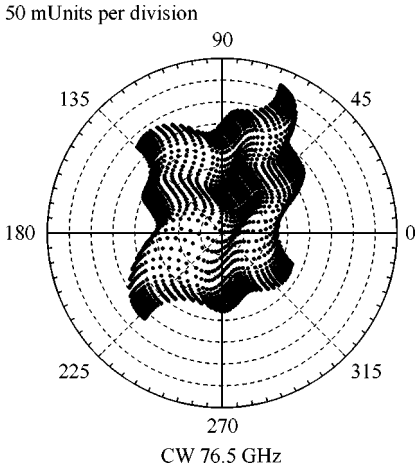

Fig. 8. Measured static constellation.

As a final note, the examples presented here are but two of many possible modulation and processing schemes that can be accommodated by the software radar architecture.

IV. Static S-Parameter Measurements

Based on the principles presented in Section II, a 76.5-GHz vector modulator was designed using microstrip on 100-μm-thick GaAs. The final MMIC, shown in Fig. 7, was fabricated by Marconi Caswell Limited, using their H40 process. It has dimensions of 2 mm $\times$ 1.6 mm. With the exception of the short 50-Ω interconnecting lines, at the input and output of the push–pull (bi-phase) modulators, the MMIC is completely represented by the expressions given in Section II. These omitted elements are significant, but since they affect both the in-phase and quadrature channels equally, they simply attenuate and shift the phase of the overall response without introducing any distortion. One additional advantage of this vector modulator is that it can be fabricated on a process that is for significantly lower frequency designs. Although the H40 process is technically limited to designs below 40 GHz, the vector modulator is able to exceed this boundary because it is biased to operate in a passive mode.

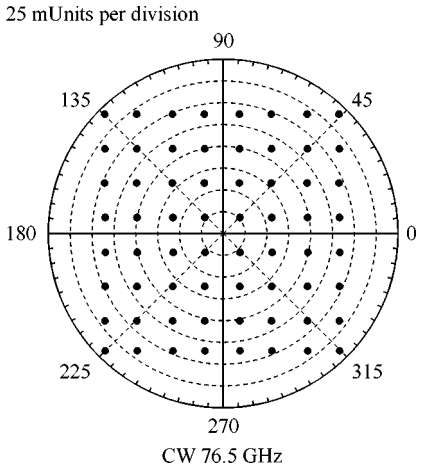

Fig. 9. Extracted 64-QAM constellation.

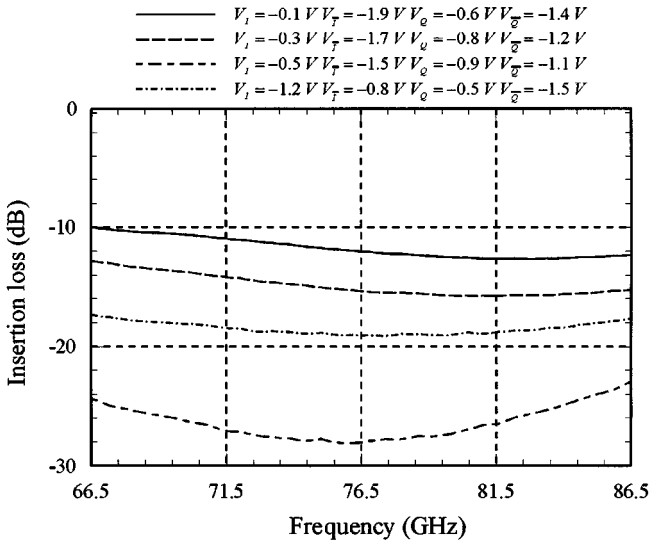

Fig. 10. Transmission response versus frequency.

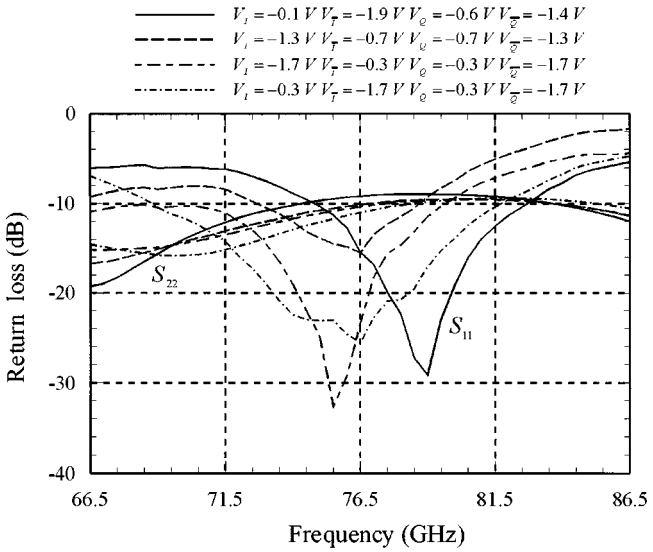

Fig. 11. Input/output return loss versus frequency.

In previous studies of vector modulators, static S-parameter measurements are typically presented in terms of ideal calibrated constellations [1]–[5]. Although this is suitable for demonstrating that such constellations are possible, it does little to expose the underlying behavior of the circuit itself. The complete range of transmission states for this vector modulator is shown in Fig. 8. The results were obtained by sweeping the I and Q control voltages (and their complements) over a two-dimensional array using a computer-controlled measurement setup. Both the in-phase and quadrature control inputs were swept from -2 to 0 V, in steps of 0.016 V, giving an array of 16 384 points. For clarity, only one-quarter of these points are actually plotted in Fig. 8. From this figure, the various amplitude and phase imbalances become apparent. In particular, the entire dataset appears shifted toward the first quadrant, and the third quadrant is rather sparse. This means that, for modulated waveforms, the effective insertion loss is only as good as the worst quadrant. Having sampled such a large range of data, it now becomes simple to extract specific static constellations. For 64 QAM, the desired amplitude and phase states are specified and a computer program is used to search through the data to find the best possible match at each constellation point. Applying this approach, the 64-QAM constellation for the vector modulator is shown in Fig. 9.

The magnitude of the transmission response is plotted in Fig. 10 as a function of frequency (66.5–86.5 GHz). In order to avoid cluttering the figure with curves, only four representative responses are given. These correspond to four different transmission levels. For the lowest insertion loss, i.e., 12 dB, the variation with frequency is approximately ± 0.1 dB over a 1-GHz bandwidth. This increases to approximately ± 1 dB at the highest insertion loss state. The input and output return losses are shown in Fig. 11 where each one of the four states represents the response in a different quadrant. The worst-case input return loss is 15 dB and the worst-case output return loss is 8 dB.

The static constellations and frequency responses for the vector modulator were measured using an Agilent 8510XF vector network analyzer and a Cascade Summit 9000 on-wafer probe station.

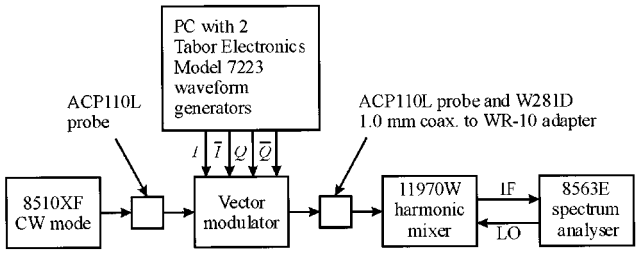

Fig. 12. Spectrum measurement setup.

V. Measured Modulation Spectra

Based on the static constellation measurements, three different output waveforms were generated from the vector modulator: FMCW, 64-QAM, and small-shift frequency translation (SSFT). A pair of two-channel Tabor Electronics Ltd. Model 7223 PC-based waveform generators were used to generate the baseband signals, as shown in the measurement setup of Fig. 12.

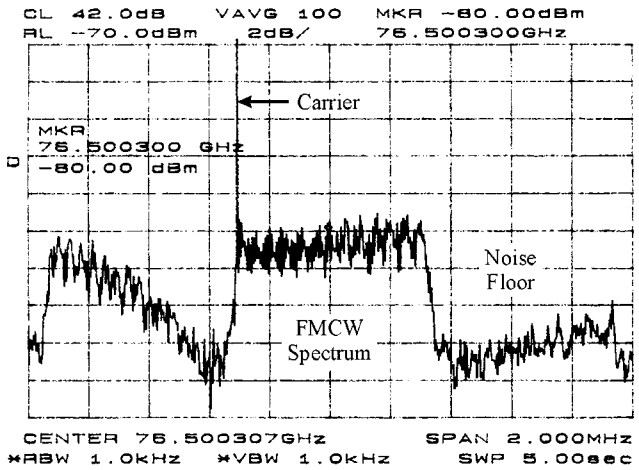

Fig. 13. FMCW spectrum.

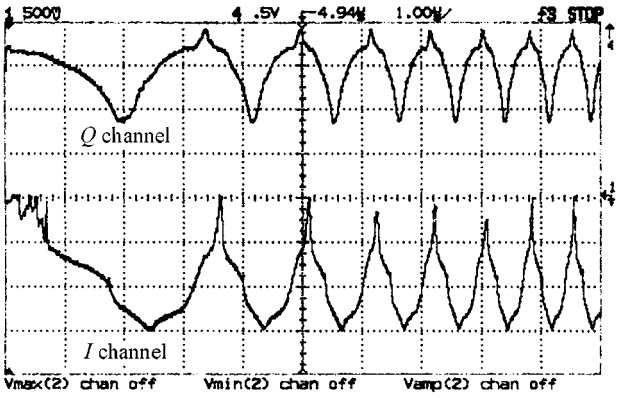

Fig. 14. I and Q baseband signals for FMCW.

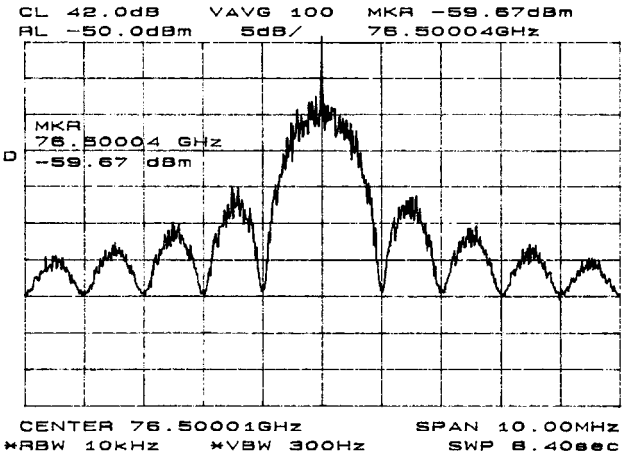

Fig. 15. 64-QAM spectrum.

Each unit can generate two independent 12-bit arbitrary signals that are specified by a data file with a maximum sample rate of 50 Msamples/s. By synchronizing two generators together, it is possible to generate the required complementary signal pairs for the I and Q channels. The 76.5-GHz carrier is generated using the CW mode on the Agilent 8510XF vector network analyzer and injected into the vector modulator using Cascade ACP110L 1.0-mm coaxial probes. The resulting modulated signal is then extracted from the chip using a similar probe, injected into a W-band harmonic mixer via a 1.0-mm to WR-10 adapter and displayed on an Agilent 8563E spectrum analyzer.

For the FMCW demonstration, a 32 678 sample sequence was extracted from the measured static constellation. The procedure is to specify the required value of the complex transmission coefficient for every sample and then to search through the static constellation data until each point is matched with an equivalent measured value. The desired transmission response as a function of time is given by

$$S_{21}(t) = A\left[\cos\left(\frac{\mu t^2}{2}\right) + j\sin\left(\frac{\mu t^2}{2}\right)\right] \tag{42}$$

where A is an amplitude correction term to accommodate for the fixed insertion loss of the vector modulator. Once the optimal measured value for each sample is known, a list of sequenced control voltages can be generated. For FMCW, the maximum bandwidth that can be digitally generated is limited by the Nyquist sample rate, which is one-half of the waveform generator's maximum sample rate (in this case, 25 MHz). However, the resulting waveform is highly distorted. In order to reduce the distortion and represent the highest frequencies in the linear ramp clearly, it is necessary to oversample. The frequency ramp rate μ (rad/s^2) can be calculated from

$$\mu = \frac{2\pi(f_{\text{sample}})^2}{MN} \tag{43}$$

where f_{sample} is the sample rate, M is the oversampling factor, and N is the total number of samples in the sequence. Figs. 13 and 14 show the FMCW spectrum and corresponding I and Q baseband waveforms for the case that $f_{\text{sample}} = 10$ Msamples/s, $M = 16$, and $N = 2^{15}$. This yields a waveform with a (10 Msamples/s)/16 $= 625$ kHz bandwidth. From Fig. 13, spectral features are apparent. Firstly, the presence of the carrier indicates that the isolation of the Lange couplers, discussed in Section II, is insufficient and leads to a significant leakage path. Secondly, the presence of a partial lower sideband suggests that the I and Q channels are not sufficiently synchronized with each other to provide the required cancellation. This problem is not inherent to the concept of the vector modulator; rather, it is a fault with this *specific* measurement setup. By improving the synchronization and reducing the oversampling rate slightly, a wider bandwidth is possible. For the automotive radar application, the required range resolution is less than 0.5 m, which requires bandwidths of the order of several hundreds of megahertz. Although waveform generators capable of these bandwidths exist, they are currently expensive and consume prohibitive amounts of power. Nevertheless, low-cost low-power units may be available in the future.

Fig. 15 shows the 64-QAM spectral response of the vector modulator with the corresponding I and Q baseband signals shown in Fig. 16. The symbol rate was 1 Msample/s, giving an equivalent data rate of 6 Mb/s for 64 QAM operating at a frequency of 76.5 GHz. The main purpose of this experiment was to demonstrate that the same vector modulator generating an FMCW signal could be adapted to generate a polyphase code. 64 QAM was chosen because it exhibits an easily identifiable spectral response in the absence of any pulse shaping.

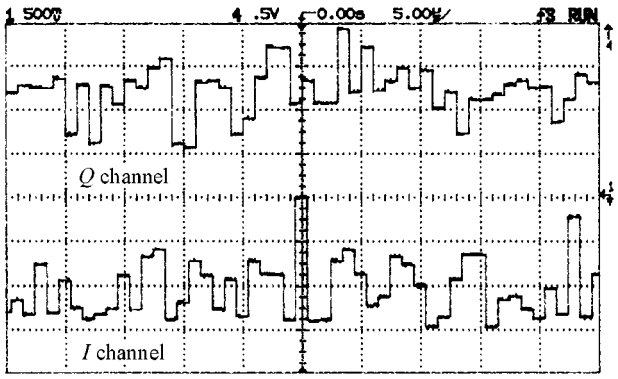

Fig. 16. I and Q baseband signals for 64 QAM.

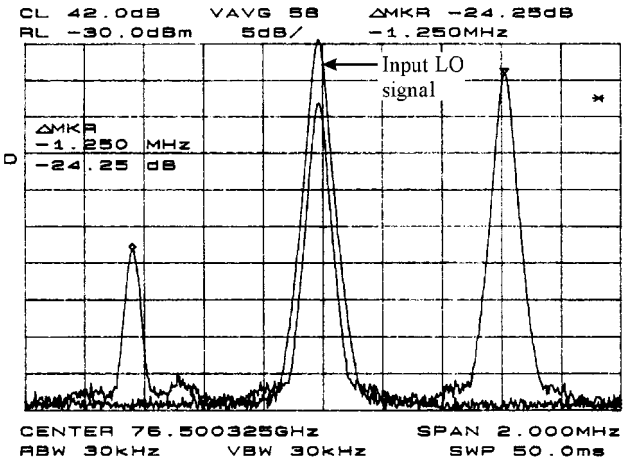

Fig. 17. SSFT spectrum.

The final measured spectrum demonstrates the vector modulator's ability to perform SSFT. This has recently been shown to be an ideal technique for performing channel selection in a millimeter-wave software radio [3]. SSFT is effectively a single-sideband modulation that results in a tone appearing above or below the suppressed carrier. In terms of the I–Q vector modulator, the required baseband signals can be derived as follows:

$$\begin{aligned} v(t) &= \cos\Big[2\pi(f_{\rm LO}+f_{\rm shift})t\Big] \\ &= \cos\Big[2\pi f_{\rm shift}t\Big]\cos\Big[2\pi f_{\rm LO}t\Big] \\ &\quad -\sin\Big[2\pi f_{\rm shift}t\Big]\sin\Big[2\pi f_{\rm LO}t\Big]. \end{aligned} \tag{44}$$

From whence the baseband I and Q signals can be extracted

$$I=\cos\big(2\pi f_{\rm shift}t\big) \text{ and } Q=\sin\big(2\pi f_{\rm shift}t\big). \tag{45}$$

When applied to the vector modulator's I and Q channels, the result is to shift the carrier by an amount equivalent to $f_{\rm shift}$. From a digital perspective, the maximum amount of frequency shift is limited, by the amount of oversampling and the waveform generators sample rate. In this example, a full sweep of 2π was performed in 16 samples, permitting an effective frequency shift 1/16th of the sample rate. Using the waveform generator's maximum sample rate of 50 Msamples/s, this results in a shift of 3.125 MHz. The SSFT spectrum and predistorted baseband control signals are shown in Figs. 17 and 18, respectively. From

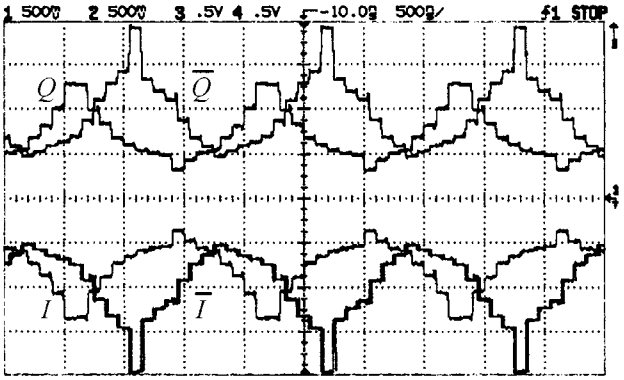

Fig. 18. I and Q baseband signals for SSFT.

Fig. 17, the lower sideband rejection is 24 dB. It can also be seen that the original local oscillator (LO) signal is still present after the SSFT is applied. This is due to inadequate Lange coupler isolation.

VI. Conclusions

The I–Q (push–pull) vector modulator is an ideal circuit for use in software radar. Without changing the front-end hardware, it enables the radar to adapt between modulating waveforms simply by changing the data stored in the memory of the arbitrary waveform generators and by reprogramming the baseband receiver electronics. The vector modulator itself is quite simple to design, as it is merely an arrangement of couplers and cold pHEMTs. Furthermore, it is compact and promises to have high yield because the devices are biased in a resistive mode. The degradation in modulation performance can also be minimized. Following a detailed theoretical analysis of the circuit, the principal sources of degradation have been attributed primarily to imperfections in the couplers and practical limitations of the variable resistive elements. With better couplers and suitably designed pHEMT devices, the performance of the vector modulator could be substantially improved.

Acknowledgment

The authors would like to thank Marconi Caswell Limited, Caswell, U.K., for access to their foundry.

References

[1] S. Lucyszyn and I. D. Robertson, "Vector modulators for adaptive and multi-function microwave communication systems," in *Proc. Microwaves'94 Conf.*, London, U.K., pp. 103–106.

[2] S. Lucyszyn, T. Sewell, and I. D. Robertson, "Multi-level digital modulation performed directly at carrier frequency," in *Proc. 25th European Microwave Conf.*, Bologna, Italy, Sept. 1995, pp. 673–676.

[3] M. Chongcheawchamnan, K. S. Ang, D. Kpolga, S. Nam, S. Lucyszyn, and I. D. Robertson, "Low-cost millimeter-wave transmitter using software radio techniques," in *IEEE MTT-S Int. Microwave Symp. Dig.*, Boston, MA, June 2000, pp. 1949–1952.

[4] A. E. Ashtiani, S. Nam, A. d'Espona, S. Lucyszyn, and I. D. Robertson, "Direct multilevel carrier modulation using millimeter-wave balanced vector modulators," *IEEE Trans. Microwave Theory Tech.*, vol. 46, pp. 2611–2619, Dec. 1998.

[5] S. Nam, N. Shala, K. S. Ang, A. E. Ashtiani, I. D. Robertson, and S. P. Marsh, "Monolithic millimeter-wave balanced bi-phase amplitude modulator in GaAs/InGaP HBT technology," in *IEEE MTT-S Int. Microwave Symp. Dig.*, Anaheim, CA, June 1999, pp. 243–246.

[6] J. R. Lamberg, M. J. Gawronski, J. J. Geddes, W. R. Carlyon, and R. A. Hart, "A compact high performance W-band FMCW radar front-end based on MMIC technology," in *IEEE MTT-S Int. Microwave Symp. Dig.*, Anaheim, CA, June 1999, pp. 1797–1800.
[7] H. J. Siweris, A. Werthof, H. Tischer, U. Schaper, A. Schäfer, L. Verweyen, T. Grave, G. Böck, M. Schlechtweg, and W. Kellner, "Low-cost GaAs pHEMT MMIC's for millimeter-wave sensor applications," *IEEE Trans. Microwave Theory Tech.*, vol. 46, pp. 2560–2567, Dec. 1998.
[8] K. W. Chang, H. Wang, G. Shreve, J. G. Harrison, M. Core, A. Paxton, M. Yu, C. H. Chen, and G. S. Dow, "Forward-looking automotive radar using a W-band single-chip transceiver," *IEEE Trans. Microwave Theory Tech.*, vol. 43, pp. 1659–1668, July 1995.
[9] M. Camiade, D. Domnesque, P. F. Alleaume, A. Mallet, D. Pons, and H. Dämbkes, "Full MMIC millimeter-wave front-end for a 76.5 GHz adaptive cruise control car radar," in *IEEE MTT-S Int. Microwave Symp. Dig.*, Anaheim, CA, June 1999, pp. 1489–1492.
[10] S. Lucyszyn and I. D. Robertson, "Analog reflection topology building blocks for adaptive microwave signal processing applications," *IEEE Trans. Microwave Theory Tech.*, vol. 43, pp. 601–611, Mar. 1995.
[11] S. Lucyszyn, V. Magnier, H. C. Reader, and I. D. Robertson, "Ultrawideband measurement of multiple-port MMIC's using nonideal test fixtures and a 2-port ANA," *Proc. Inst. Elect. Eng.*, pt. A, vol. 139, pp. 235–242, Sept. 1992.
[12] R. Mongia, I. Bahl, and P. Bhartia, *RF and Microwave Coupled-Line Circuits*. Norwood, MA: Artech House, 1999.
[13] H. D. Griffiths and W. J. Bradford, "Digital generation of high time-bandwidth product linear FM waveforms for radar altimeters," *Proc. Inst. Elect. Eng.*, pt. F, vol. 139, pp. 160–169, Apr. 1992.

Douglas S. McPherson (S'99–M'00) was born in Ottawa, ON, Canada, on June 21, 1973. He received the B.S. degree in engineering physics from Queen's University, Kingston, ON, Canada, in 1995, the M.S. degree in electrical engineering from Carleton University, Ottawa, ON, Canada, in 1998, and the Ph.D. degree in electrical engineering from the University of Surrey, Surrey, U.K., in 2001.

He is currently a Design Engineer with Quake Technologies Inc., Ottawa, ON, Canada. His research interests are in W-band integrated radar, millimeter-wave analog signal processing, MMICs, and nonlinear active device modeling.

Stepan Lucyszyn (M'91) was born in Bradford, U.K., in 1965. He received the Bachelors degree in electronic and communication engineering from the Polytechnic of North London, London, U.K., in 1987, the Masters degree in satellite communication engineering from the University of Surrey, Surrey, U.K., in 1988, and the Ph.D. degree in electronic engineering from King's College London, London, U.K., in 1992.

He spent one year in the British and French space industries, where he was a consultant on a broad range of projects. In 1992, he was a Post-Doctoral Research Fellow at King's College London, where he investigated advanced microwave analog signal processing. In August 1995, he became a Lecturer in RF electronics, and in April 2000, became a Senior Lecturer. In 1999, he spent three months at the Nanyang Technological University, Nanyang, Singapore. He is currently the Principal Investigator on two millimeter-wave research projects and a Co-Investigator on other projects with the Microwave and Systems Research Group, University of Surrey. He has co-authored approximately 65 research papers in both national and international conferences and journals in the area of microwave and millimeter-wave engineering. He has also contributed three chapters to *MMIC Design* (London, U.K.: IEE Press, 1995) and four chapters to *RFIC and MMIC Design and Technology* (London, U.K.: IEE Press, **19??**).

Dr. Lucyszyn was the recipient of the 1987 Departmental Prize from the Polytechnic of North London. He was also the recipient of the 1999 Tan Chin Tuan Exchange Fellowship in Engineering.